Study on evolution law of non-equilibrium phase transition flow and performance improvement of steam ejector for MED-TVC desalination system

Study on evolution law of non-equilibrium phase transition flow and performance improvement of steam ejector for MED-TVC desalination system

Yongzhi Tang [a], Zilong Zhong [a], Zhongliang Liu [b,*], Lin Lu [a], Yichen Huang [a], Chuang Wen [c,*]

a. Department of Energy Science and Engineering, Jingdezhen Ceramic University, Jingdezhen 333001, China.

b. Department of Energy Science and Engineering, Beijing University of Technology, Beijing 100124, China.

c. School of the Built Environment, University of Reading, Reading RG6 6AH, UK.

*Corresponding authors

E-mail address: liuzhl@bjut.edu.cn (Zhongliang Liu); c.wen@reading.ac.uk (Chuang Wen).

Abstract: Non-equilibrium phase transition flow is prevalent and of great irreversible loss during the transonic mixing process of steam ejector, but its complex evolution law is thus far unclear. In this study, a considerate two-phase ejector model was developed, and numerical simulations were employed to investigate the characteristics of non-equilibrium phase transition flow, including how, where and to what extent the phase transition occurs. Additionally, the influences of operating parameters on the phase transition flow and ejector's entrainment performance were comprehensively elucidated. The results showed that the evolution of condensate is highly consistent with the pressure fluctuation of shock wave. Increasing the primary fluid pressure intensifies non-equilibrium condensation, thereby worsening the entrainment performance. In contrast, raising the secondary fluid pressure has the opposite effect, with the entrainment ratio ω increasing by up to 17.8%. Superheating

the working fluids can restrain the droplet development, leading to the generation of more small-sized droplets, but ω only improves by a maximum of 3.53%. However, it is hard to restrain the condensate generation in primary jet flow by superheating the secondary fluid, both the suction pressure and the ω decrease. This study provides meaningful guidance for reducing the irreversibility loss from non-equilibrium phase transition flow.

Keywords: Steam ejector; Non-equilibrium phase transition flow; Shock wave; Performance improvement; Operating parameters analysis

Highlights:

1. Developing a considerate two-phase model to investigate the phase transition flow characteristics of condensable gas.
2. How, where and to what extent the phase transition occurs inside the steam ejector were clarified.
3. The shock wave is the primary factor influencing the distribution of the liquid phase during the mixing process.
4. The expansion wave promotes local condensate droplets to fragment, while the compression wave leads to the aggregation of droplets.
5. Influence laws of operating parameters on the phase transition flow characteristics and ejector's entrainment performance were elucidated.

Nomenclature

P_p	primary fluid pressure, kPa	r_c	droplet critical radius, m
T_p	primary fluid temperature, K	q_c	condensation coefficient

P_s	secondary fluid pressure, kPa	m_v	single vapor molecule mass, kg
T_s	secondary fluid temperature, K	k_B	boltzmann constant
P_m	back pressure, kPa	h_{lv}	latent heat of condensation, kJ/kg
T_m	mixed fluid outlet temperature, K	S	supersaturation ratio
m_p	primary fluid mass flow rate, g/s	Kn	Knudsen number
m_s	secondary fluid mass flow rate, g/s	B_1	second virial coefficient
ΔT_p	primary fluid superheat degree, K	B_2	third virial coefficient
ΔT_s	secondary fluid superheat degree, K		
P_e	entrainment passage pressure	*Greek symbol*	
ΔP_e	entrainment passage pressure difference	ρ	mixture density
Ma	Mach number	ρ_v	vapor density
f	liquid mass fraction	ρ_l	liquid density
f_a	average of liquid mass fraction	σ	liquid surface tension
f_e	entrainment passage liquid mass fraction	ω	entrainment ratio
n	number of liquid droplets	γ	specific heat ratio
J	nucleation rate, $m^{-3}s^{-1}$	Γ	liquid mass generation rate, $kg/m^3 \cdot s$
r	droplet radius, m	λ_v	thermal conductivity of vapor, W/m·K
V_d	droplet volume, m^3	μ_v	dynamic viscosity of vapor, kg/m·s
P_{sat}	saturation pressure, Pa		

1. Introduction

As global economic development progresses, energy consumption has steadily increased in the past few years, accompanied by significant carbon emissions and environmental pollution. Consequently, energy conservation and emissions reduction have emerged as crucial focal points for social sustainable development. Among environmentally friendly fluid machinery, the steam ejector is frequently appears in various thermal systems, such as the jet refrigeration cycle[1, 2], multi-effect

distillation with thermal vapor compression (MED-TVC) desalination systems[3, 4], and PEM fuel cell systems[5, 6]. This is due to its outstanding ability to effectively utilize low-grade energy without consuming any of mechanical power. Taking the MED-TVC desalination system as an example, the application of steam ejector can utilize the high-pressure potential energy of working steam to circulate non-condensable steam from the end condenser. As a result, the latent heat of non-condensable steam is recovered, and a more low-pressure distillation environment is created for each effect evaporator[7], as shown in Fig 1.

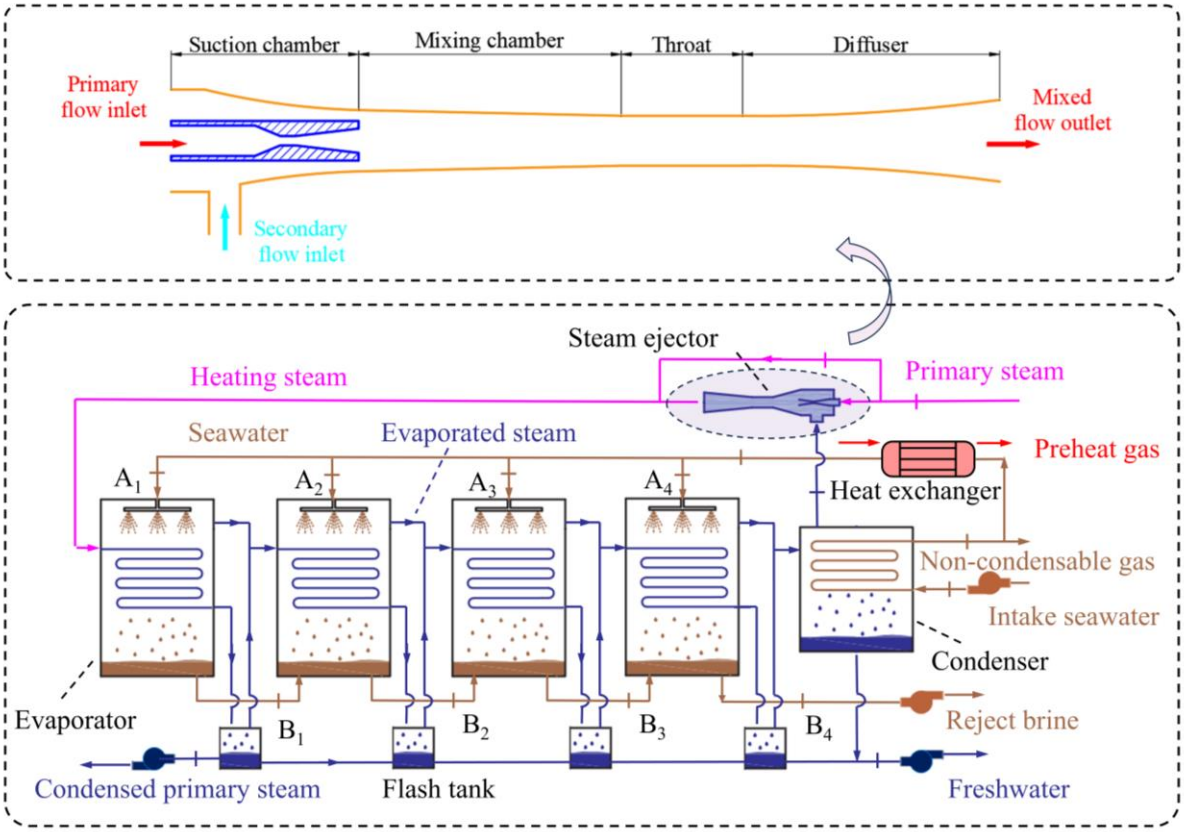

Fig.1 Schematic diagram of MED-TVC system

The superior ability of steam ejector to recover low-grade thermal energy and improve energy efficiency makes it suitable for a broader array of industrial applications, but it should be pointed out that the steam ejector often becomes the component with the greatest irreversible losses in the

associated thermodynamic system[8, 9]. This is mainly attributed to the inherent defects of the ejector design theory and the strong irreversible flow phenomena existing in the phase-changing transonic flow process. Consequently, the performance improvement of steam ejector has gained special attention of many researchers. Over the past years, many performance improvement efforts focus on the configuration parameters optimization and local structural innovation. Key areas of configuration parameters optimization comprise the primary nozzle[10, 11], mixing chamber[12], throat[13], and innovations in local structural components include the auxiliary entrainment[14], pressure regulation[3], abnormal-shaped nozzle[15] and so on. Results have shown that structural optimization and innovation have contributed to a significant performance improvement of ejector. As a matter of fact, the deterioration of ejector's performance is often attributed to a defective flow field, which usually induces large irreversible losses. For example, the shock waves, choking flow, non-equilibrium phase transitions, vortices, and interactions within shear layers[16]. Structural optimization and innovation are essentially improvement of the internal flow field for reducing the irreversible losses. As such, gaining a thorough understanding of internal flow fields is the premise of ejector's performance improvement. Currently, the transonic mixing flow characteristics of ideal gas in the ejector have achieved a rather deep understanding, but it is far from enough for condensable gas. The main reason is that the non-equilibrium phase transition of condensable gas greatly aggravates the complexity of the transonic mixing process. Saturated steam is easy to become unstable oversaturated state during the transonic flow process inside a steam ejector. As the critical degree of supercooling (Wilson point) is reached, non-equilibrium phase transition occurs[17]. As a result, abundant condensation droplets appear, and a substantial amount of latent heat releases. The thermodynamic and

mechanical equilibriums of the local flow fields are subsequently broken. Concurrently, the condensation latent heat will heat up the surrounding fluid, causing local temperatures gradually rise, and the thermodynamic equilibrium between the two phases is restored progressively. During this process, the number of droplets ceases to increase significantly, while steam molecules continue to condense onto existing nuclei, thereby increasing the liquid mass fraction[18]. Apparently, such a supersonic phase transition jet of mechanical imbalance enters the mixing chamber to mix with the entrained fluid, which will greatly aggravate the complexity of the internal flow field under the action of shock disturbance and transonic mixing.

The non-equilibrium phase transition phenomenon[19, 20] pervades the entire flow process inside the steam ejector, often resulting in significant irreversible loss. It is a critical aspect in the study of the transonic flow characteristics of condensable gases. Zhang *et al*.[21] modified the classical nucleation model that describes surface tension solely as a function of temperature, for considering the nonlinear effects of droplet size and temperature on surface tension. Subsequently, the predictive capabilities of four different models for non-equilibrium condensation were compared, along with the flow structure and ejector performance. The results suggested that the developed modified model achieves superior suitability for predicting ejector performance, with a deviation of only 1.5% in critical condensation pressure values compared to experimental data. The high agreement between numerical simulations and the experimental results provides a reliable foundation for capturing internal flow losses and guiding optimization efforts. On this basis, Zhang *et al*.[22] introduced a Multi-Objective Genetic Algorithm (MOGA) to optimize the nozzle. Their results showed that the non-equilibrium condensation intensity within the nozzle decreases, the flow losses reduce, and the entrainment ratio

increased by approximately 27.5% after MOGA optimization. These works are of fundamental significant and offer substantial practical guidance.

The complex heat and mass transfer induced by phase change processes are fundamental to the formation of the liquid phase in transonic flows. The presence of this liquid phase significantly affects the internal flow, primarily because the formed condensate droplets alter the available flow area of the primary fluid[23], this leads to a substantial negative effect on the working performance of steam ejector [16, 24]. Yang *et al*.[25] developed a wet steam model to study the complex condensate flow characteristics inside a steam ejector and evaluate its entrainment performance. The results showed that the wet steam model has a 11.71% depreciation of entrainment ratio compared to the dry gas model, and it is of a higher prediction accuracy on the expansion characteristics inside the nozzle, the Mach number at the nozzle exit and the entrainment ratio. The primary reason for this difference is that the dry gas model, by neglecting condensation, significantly overestimates the expansion characteristics, leading to discrepancies with the actual temperature field. Wen *et al*.[26] constructed and compared single-phase and two-phase flow models to evaluate the working performance of steam ejector in the MED-TVC system. Their findings demonstrated that the single-phase flow model under-predicts the entropy loss coefficient by approximately 15%, while the two-phase model exhibits higher accuracy. Apparently, non-equilibrium condensation has a significant impact on the working performance of steam ejectors when condensable gas is used as the working medium. Wen *et al*.[27] further focused on the non-equilibrium condensation processes of steam ejector. Their results revealed that, with higher suction chamber pressure, the flow transitions form an under-expanded to an over-expanded state, leading to a significant increase in steam entrainment and entropy loss. Ding *et al*.[28]

utilized a wet steam model to study the effects of phase transition on the development of two-phase mixing layer in a desalination-oriented ejector. They found that the formation and flow of condensate droplets hindered the development of mixing layer. As a result, the mixing layer length predicted by the dry model exceeded that of the wet model by 25.1%.

Moreover, Aliabadi and Bahiraei[29] investigated the influences of liquid droplets in primary steam on various two-phase parameters, shock waves, entrainment ratio, mixing layer growth, and two-phase heat transfer. The study results indicated that at the nozzle inlet humidity of 0.4%, the condensation shock is delayed the most. At this point, the liquid mass fraction, temperature, entrainment ratio, and mixing boundary growth at the nozzle exit all reach their minimum values. As the inlet humidity further increases, these parameters rise, while the Mach number decreases. A similar conclusion was drawn in Feng's study[30], where a 9.15% decrease in the ejector's entrainment ratio occurred as the droplet mass fraction increased from 0 to 0.12. This was accompanied by a significant reduction in condensation intensity at both the nozzle throat and exit. Ding *et al*.[31] developed a two-phase non-equilibrium hydrogen recirculation ejector model to investigate the effects of phase transition on ejector performance under various operating conditions. Their findings revealed that increasing the primary pressure from 3.0 bar to 5.0 bar caused the outlet liquid mass fraction to change from 4.56% to 15.35%. Exergy destruction increased as primary fluid pressure rose, while higher secondary pressures had the opposite effect. Ghorbani *et al*.[32] performed operating parametric analysis and multi-objective optimization study on a MED-TVC system. The results revealed that the entrainment ratio increases with higher secondary pressures, and the back pressure plays a crucial role in defining the operational range of the TVC system. Moreover, Tang *et al*.[24] proposed a double-

choking theory that considers condensing flow to investigate the relationship between two-phase choking flow and the ejector's entrainment performance. The results indicated that the formation and flow of condensate have significant negative effects on the entrainment performance of steam ejector. Additionally, the phase transition flow loss area is larger than the entrainment choking area in most cases, and it enlarges with the higher primary and entrained steam pressures.

Numerical simulations give a comprehensive understanding of the non-equilibrium phase transition characteristics and their influence on the working performance of steam ejectors. Most numerical studies are thus far limited to non-equilibrium phase transition characteristic within the primary nozzle and the simple distribution of the gas-liquid phase within the steam ejector. However, existing two-phase models are powerless for simulating phase transition properties, such as heat and mass transfer, liquid phase evolution, and mixing mechanism during transonic mixing processes inside steam ejector. For a deeper understanding of these phenomena, visualization experiments are proposed accordingly. Tang *et al*.[16] established a visualization experimental platform to study the formation mechanisms and evolutionary patterns of condensing flow. Their results revealed that an inhomogeneous size distribution and dynamic imbalance of condensation droplets within the supersonic jet flow. A distinct inclined condensate choking cross-section was observed at the end of the mixing chamber. The condensate flow pattern and quantity varied with different observation views and operating parameters, with large droplets tending to accumulate below the axis. Additionally, a quite complex flow process appears upstream of the choking cross-section that covers flexible vortices, clockwise annular flows, and condensate accumulation. Li *et al*.[33] launched the visual experiments on CO_2 trans-critical phase transition flow and accurately captured the phase-change location within

the primary nozzle. The results revealed that as the primary fluid pressure decreases, the phase-change location shifts upstream, gradually approaching the nozzle throat. These findings are consistent with predictions based on isentropic expansion theory and changes in nozzle pressure distribution trends. Palacz *et al*.[34] developed a visualization test rig for the R744 (CO_2) two-phase ejector. It is found that the expansion angle increases with higher primary fluid mass flow rates. Additionally, the unstable operation of the ejector mixing section, caused by pressure fluctuations, leads to a decrease in the mass flow rate inside the suction chamber.

So far, researchers have devoted significant efforts to investigating the formation and evolution law of phase transition characteristic within ejectors, yielding numerous valuable results. However, there is only a shallow understanding of the phase transition flow characteristic during the transonic mixing process of two condensable gases, and the numerical visualization of this aspect is particularly poor. In this study, a considerate two-phase model was developed to conduct an in-depth analysis towards the formation and development of phase transition flow within the desalination-oriented steam ejector. The study also explores the influences of operating parameters on the phase transition flow characteristic and ejector performance. Furthermore, fundamental links between operating parameters, phase transition effects and entrainment performance of ejector are established. This work holds significant theoretical and practical importance, contributing to the development of suppression measures for phase transition flow and the enhancement of steam ejector performance.

2. Mathematical models

2.1 *Governing equations*

The fluid flow within a steam ejector must first satisfy a set of fundamental governing equations, including the continuity equation, momentum equation, and energy equation.

The continuity equation:

$$\frac{\partial \rho}{\partial t} + \frac{\partial}{\partial x_i}(\rho u_i) = 0 \tag{1}$$

The momentum equation:

$$\frac{\partial}{\partial t}(\rho u_i) + \frac{\partial}{\partial x_j}(\rho u_i u_j) = -\frac{\partial p}{\partial x_i} + \frac{\partial \tau_{ij}}{\partial x_j} \tag{2}$$

The energy equation:

$$\frac{\partial}{\partial t}(\rho E) + \frac{\partial}{\partial x_i}[u_i(\rho E + p)] = \vec{\nabla}(\lambda_e \frac{\partial T}{\partial x_i}) + \vec{\nabla}[u_j(\tau_{ij})] \tag{3}$$

The non-equilibrium phase transition process within the steam ejector is characterized by two transport equations: one for the liquid mass fraction (f) and another for the liquid droplets number (n):

$$\frac{\partial(\rho f)}{\partial t} + \frac{\partial}{\partial x_j}(\rho f u_j) = \Gamma \tag{4}$$

$$\frac{\partial(\rho n)}{\partial t} + \frac{\partial}{\partial x_j}(\rho n u_j) = \rho J \tag{5}$$

The relationship between the mixture density ρ and the vapor density ρ_v can be expressed as:

$$\rho = \frac{\rho_v}{1 - f} \tag{6}$$

The droplet number n is defined as follows:

$$n = \frac{f}{(1-f)V_d\left(\frac{\rho_l}{\rho_v}\right)} \tag{7}$$

where ρ_l is the liquid density, and the droplet volume V_d can be written as:

$$V_d = \frac{4}{3}\pi r^3 \tag{8}$$

where r is the droplet radius.

In this paper, a two-phase model is developed based on the assumption of homogeneous nucleation. The droplet nucleation and growth process of condensable gas is described using the non-isothermal droplet nucleation rate model corrected by Kantrowitz and Gyarmathy's droplet growth model. The approach fully accounts for the interactions between liquid droplets and surrounding gas phase during phase transition, as well as the effect of the low-pressure flow environment. The property of condensable gas is characterized using the wet steam state equation. Details are as follows.

(I) The non-isothermal droplet nucleation rate model corrected by Kantrowitz[35]:

$$J = \frac{q_c}{1+\phi}\frac{\rho_v^{\,2}}{\rho_l}\sqrt{\frac{2\sigma}{\pi m_v^{\,3}}}\exp(-\frac{4\pi\sigma}{3k_BT_v}r_c^{\,2}) \tag{9}$$

where the condensation coefficient q_c is 1, the single vapor molecule mass m_v is 3×10^{-26} kg, and the Boltzmann constant k_B is 1.38×10^{-23} J/K. The non-isothermal correction coefficient ϕ and the droplet critical radius r_c, they can be written as[38]:

$$\phi = \frac{2(\gamma-1)}{(\gamma+1)}\frac{h_{lv}}{RT}(\frac{h_{lv}}{RT}-\frac{1}{2}) \tag{10}$$

$$r_c = \frac{2\sigma}{\rho_l RT\ln S} \tag{11}$$

where γ is specific heat ratio, h_{lv} is the latent heat of condensation, and σ is the liquid surface tension evaluated at temperature as follow[28]:

$$\sigma = 0.2358\left(1-\frac{T}{647.286}\right)^{1.256}\cdot\left[1-0.625\left(1-\frac{T}{647.286}\right)\right] \tag{12}$$

and the supersaturation ratio S is calculated as follows.

$$S = \frac{P}{P_{sat}} \tag{13}$$

where P_{sat} is saturation pressure.

(II) Gyarmathy's droplet growth model[36]:

$$\Gamma = \frac{4\pi r_c^{\,3}}{3}\rho_l J + 4\pi r^2 \rho_l n \frac{dr}{dt} \tag{14}$$

$$\frac{dr}{dt} = \frac{\lambda_v (T_s - T_v)}{\rho_l h_{lv} r(1+3.18\mathrm{Kn})} \tag{15}$$

where, λ_v is thermal conductivity of vapor, the Knudsen number Kn is calculated as follows:

$$\mathrm{Kn} = \frac{\bar{l}}{2r} \tag{16}$$

And, the free path of saturation vapor molecules $\bar{l}$ is formulated as follows:

$$\bar{l} = \frac{1.5\mu_v\sqrt{RT_v}}{P} \tag{17}$$

where μ_v is dynamic viscosity of vapor.

(III) Wet steam state equation[37]:

$$P = \rho_v RT(1+B_1\rho_v + B_2\rho_v^2) \tag{18}$$

where B_1 and B_2 are the second and third virial coefficients, respectively, and are functions of temperature.

2.2 *Numerical schemes*

ANSYS FLUENT 15.0 is employed for computational simulations. The UDF (User Defined

Function), written in C code, is utilized to model the non-equilibrium condensation process. A density-based solver and implicit second-order upwind discretization scheme are employed. The *k-ω* SST model is selected as the turbulence model, which has been fully validated in previous studies for its high predictive accuracy of global and local flow phenomena in supersonic two-phase flow, as well as its effective prediction of fluid mixing [39, 40]. To effectively manage the turbulent wall-bounded shear layer, the center of the first computational grid cell must be placed within the viscous sublayer to ensure the applicability of wall functions. The dimensionless distance y^+ is kept below 1. Pressure boundary condition was applied at all inlets and outlet of the steam ejector. The walls were set as adiabatic, no-slip boundary conditions. The relevant boundary conditions are summarized in Table 1. The numerical solution was considered converged when the iterative residuals of the conservation equations were less than 10^{-6}, and the iterative residuals of the mass flow rate at the ejector inlets and outlet were less than 10^{-5}.

Table 1 Inlet and outlet boundary conditions

Case	Parameters	Design parameters	Variable parameters
A	primary fluid pressure P_p (kPa)	500	460 ~ 500
B	secondary fluid pressure P_s (kPa)	20	16 ~ 24
C	back pressure P_m (kPa)	40	–
D	primary fluid superheat degree ΔT_p (K)	0	10 ~ 50
E	secondary fluid superheat degree ΔT_s (K)	0	10 ~ 50

2.3 *Grid division and independence verification*

In this study, the geometric dimensions of the steam ejector, as designed in our previous research, are adopted[14]. The steam ejector is simplified into a two-dimensional axisymmetric structure[41], and its dimensions are detailed in Fig. 2. A Block-structured meshing method was selected based on

the flow channel geometry of steam ejector. To enhance the accuracy of phase change flow capture within the ejector, grid refinement was applied near the nozzle, throat wall, and fluid mixing region in the mixing chamber. The generated mesh is presented in Fig. 3. Additionally, the number of grids is critical for both computational speed and accuracy. Four different grid densities were adopted to conduct the mesh independence verification, aiming to achieve a good balance between the two factors. The independence verification results are shown in Table 2. As one can see, the errors in the four various evaluation indicators between 204603 and 109511 grids are strictly within 0.5%. Therefore, 109511 grids is the optimal solution for simulating the designed ejector.

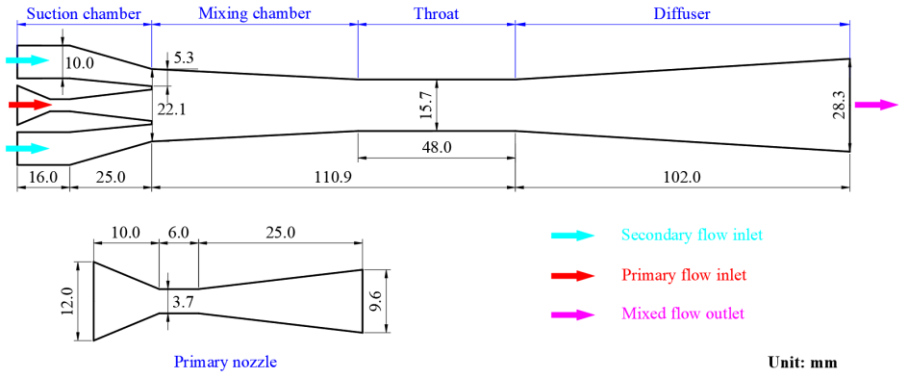

Fig.2 Detailed dimension for the steam ejector

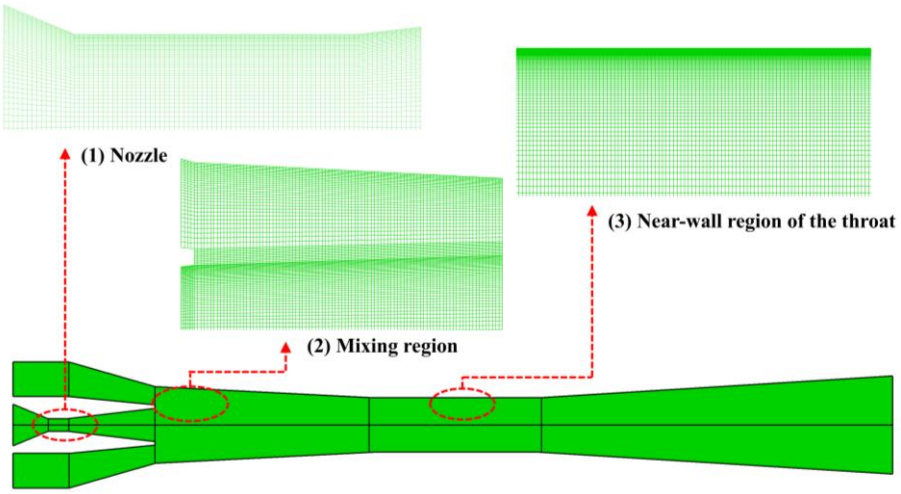

Fig.3 Computational mesh of steam ejector

Table 2-a Independence verification results of grids on the flow field of nozzle outlet

Number of grids	Pressure (kPa)	Error (%)	Velocity (m/s)	Error (%)
34494	13010	-	1092.72	-
61788	13011.51	0.011	1093.27	0.050
109511	12959.71	0.398	1095.94	0.244
204603	12999.01	0.303	1094.57	0.125

Table 2-b Independence verification results of grids on the mass flow rates

Number of grids	m_p (g/s)	Error (%)	m_s (g/s)	Error (%)
34494	7.6231	-	4.9121	-
61788	7.6206	0.032	4.9250	0.263
109511	7.6114	0.121	4.9598	0.708
204603	7.6121	0.009	4.9382	0.437

2.4 *Model reliability verification*

To validate the simulation accuracy and reliability of the above numerical model, pressure experimental data are chosen as the benchmark for validation. One is from the Laval nozzle designed by Moses-Stein[42], and other from the ejector designed by Al-Doori[43]. The comparison between numerical simulations and experimental tests under the same boundary conditions is illustrated in Fig. 4. The careful consideration of experiment factors ensures that the simulations remain highly consistent with the experimental results. Specifically, Moses-Stein et al. ensured the reliability of the data through factors such as steam purity, measurement accuracy and system stability. Similarly, Al-Doori et al. obtained experimental data while accounting for measurement uncertainty, systematic errors, and system stability. It clearly demonstrates that the predicted values from the numerical simulations align well with the experimental data, with an average relative error of less than 6%.

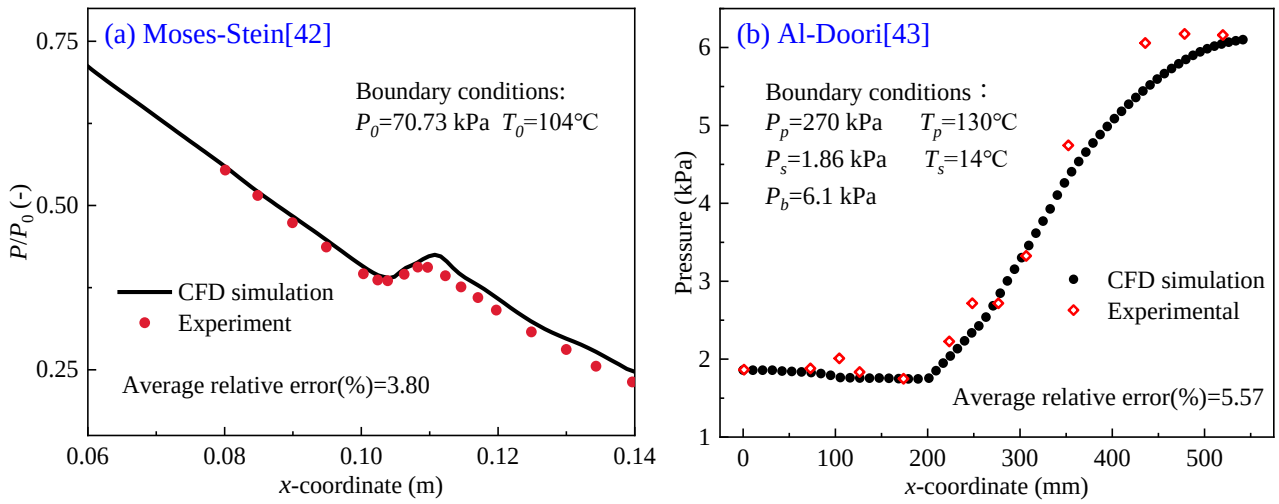

Fig. 4 Comparison results of numerical simulations versus experimental tests

3. Transonic mixing flow characteristics of condensable gas inside steam ejector

This section analyzes the transonic mixing flow characteristics of condensable gas inside the steam ejector based on the design parameters, i.e., the primary fluid pressure P_p=500 kPa, the secondary fluid pressure P_s=20 kPa, the back pressure P_m=40 kPa, and inlet fluid temperatures that are being saturated at corresponding pressure. The boundary conditions are shown in Table 1.

3.1 *Phase transition flow characteristics inside steam ejector*

Fig. 5 illustrates the pressure and Mach number contours of the steam ejector under design parameters. It is important to note that the speed of sound of the two-phase flow is determined by the relative fraction of the gas and liquid phases, combined with the mass-weighted average of their respective speed of sound. It is shown that the high-pressure working fluid realizes the acceleration from subsonic to supersonic speed within the main nozzle, causing a sharp pressure drop due to rapid expansion. At the nozzle exit, a distinct low-pressure zone and supersonic jet flow are formed, resulting in a substantial pressure difference relative to the secondary fluid. This pressure difference draws the secondary fluid into the mixing chamber, where it mixes with the supersonic jet flow along the path.

The mixed flow consists of subsonic secondary fluid surrounding the central supersonic jet flow. Consequently, a prominent mixing layer forms at the interface of the two streams, driven by strong velocity shear effects. Intense mixing within this layer primarily manifests as heat and mass exchange, with the velocities of both streams gradually becoming uniform as mixing progresses. As the mixed fluid encounters the high back pressure, its velocity decreases rapidly, and its kinetic energy is converted into pressure potential energy before exiting the ejector.

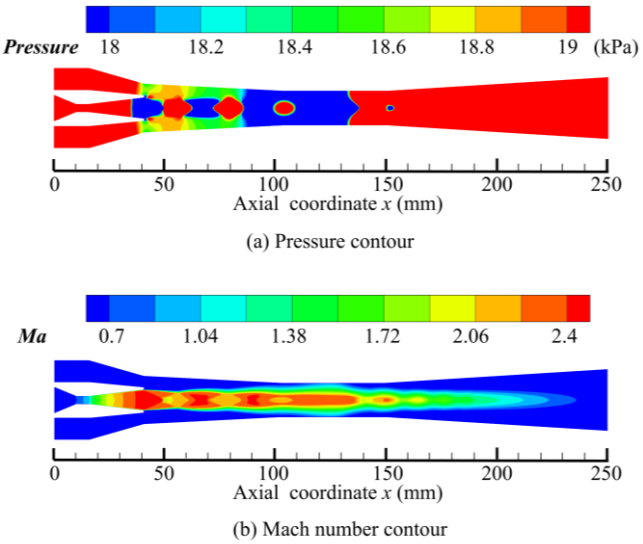

Fig.5 Distributions of pressure and Mach number within the steam ejector under design parameters

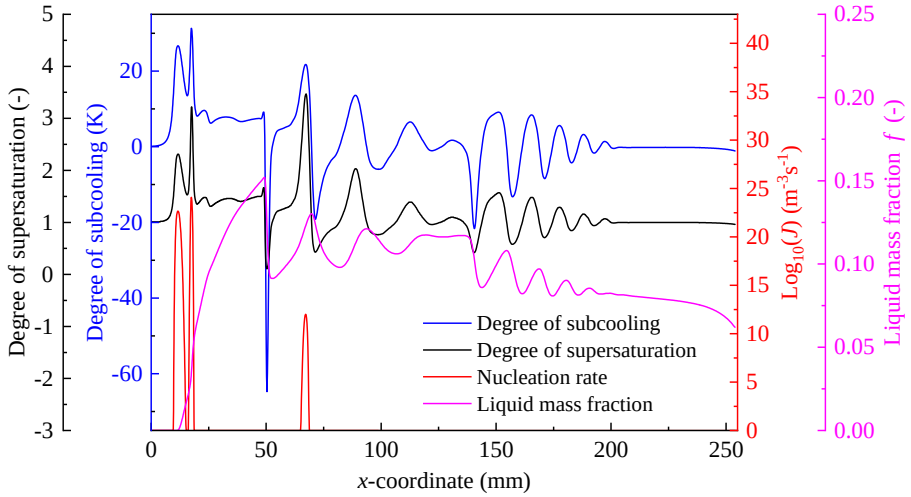

Fig.6 Distributions of degree of subcooling, nucleation rate *J*, degree of supersaturation and liquid mass fraction *f* within steam ejector under design conditions

Fig. 6 reveals the distributions of supersaturation degree, subcooling degree, nucleation rate J, and liquid mass fraction f within nozzle. It is apparent that two obvious condensate nucleation occur near the nozzle throat, with the maximum nucleation rate reaching as high as 1.22×10^{24} $m^{-3}s^{-1}$. As a result, condensate formation begins and increases. During the transonic expansion process of primary fluid (before x=41 mm), the supersaturation and subcooling degrees sharply increase first, followed by two significant fluctuations. The main reason is that large latent heat is released during instantaneous condensate nucleation, which heats both the liquid droplets and the surrounding steam. As a result, the supercooling degree decreases sharply, leading to a deterioration or even destruction of the nucleation conditions. One thing that should be pointed out is that ongoing expansion of the primary fluid significantly mitigates the negative effects of the latent heat released during condensation. While steam molecules can grow on the surface of the liquid droplets, the conditions for nucleation are no longer sustained. Finally, the supersaturation and subcooling degrees approach a plateau due to the combined effects of expansion and the latent heat from condensation. During this process, the liquid mass fraction f continued to increase rapidly, and its enlargement is attributed to the droplet growth, rather than the condensate nucleation. As for the transonic mixing process of two streams, the supersaturation degree, subcooling degree and f are fluctuating up to the end of the diffuser. Obviously, the thermodynamic state of the mixed fluid is unstable, sometimes being subcooling/supersaturation, and sometimes being superheating/unsaturation. Interestingly, a secondary condensate nucleation phenomenon appears at the front end of the mixing chamber. This condensate nucleation is not a special case of non-equilibrium condensation process in the mixing chamber, but rather an objective existence, as long as the subcooling conditions available for its nucleation are achieved. The expansion effect of expansion

waves on the shock chain provides the possibility of this phenomenon, if the expansion wave strength is strong enough. Overall, *f* presents a fluctuating decreasing trend during the transonic mixing process, ultimately dropping to 0.062 at the diffuser outlet.

3.2 *Phase transition mechanism and condensate evolution inside mixing chamber*

To compensate for the shortcomings of the knowledge on the two-phase flow characteristics and phase transition mechanism in the transonic mixing process, Fig. 7a illustrates the distribution of droplet radius *r*, axial fluid pressure, liquid mass fraction *f* and droplets number *n* within the mixing chamber. As one can see, *r* and fluid pressure maintain the same fluctuation pattern, *f* and *n* are the same, but the two groups are quite opposite. The decrease of fluid pressure facilitates condensate generation, causing *f* to increase accordingly. In turn, the increase of fluid pressure will cause the condensate to evaporate. This phenomenon can be well understood by considering the alternating occurrences of expansion and compression waves in the shock chain, which create local regions of subcooling and superheating (see Fig.6), in addition to the fluctuation of pressure. Fluid subcooling will facilitate the growth of local droplets, and if the degree of overcooling is large enough, the secondary nucleation occurs. Conversely, fluid superheating leads to the evaporation of the condensate droplets. One meaningful finding is that *r* does not enlarge with lower fluid pressure, but decreases, while *n* increases to some extent. It can be found after in-depth analysis that the expansion effect of expansion waves on the shock chain will promote the fragmentated of the local condensate droplets, and thus more small-size droplets are generated. In turn, the local condensate droplets to be aggregated when converted into a compression wave, and fewer large-size droplets appear, although the local fluid overheating intensifies the evaporation of droplets. Overall, *f* and *n* decrease along the path inside the

mixing chamber. The greater the fluid pressure fluctuation is, the more significant fluctuations of r, n and f occur.

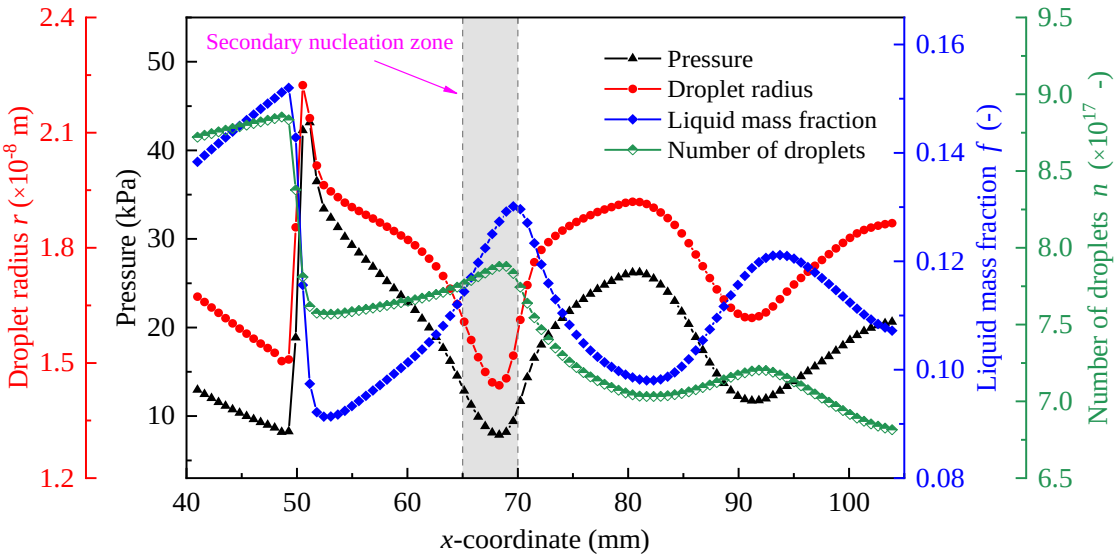

Fig.7a Distributions of droplet radius r, axial pressure, liquid mass fraction f and number of droplets n within mixing chamber

In many previous studies, the decrease in f has often been simplistically attributed to the release of latent heat of condensation. However, the behavior of the condensate in transonic flow inside the mixing chamber may be more sensitive to shock waves, as the change law of f is highly consistent with the pressure fluctuation. The latent heat from the generation or evaporation of condensate does not affect the fluid pressure fluctuation law directly, but only suppresses the rate of fluid pressure change. To be specific, as the fluid enters the compression stage, its pressure rises rapidly. This leads to local overheating of the fluid, causing some droplets to evaporate and absorb heat. The rise in local fluid pressure is partially inhibited. When the fluid enters the expansion stage, the situation is the opposite. As a result, here the amplitude of pressure fluctuations on the shock chain is smaller than that predicted by the single-phase model. This point can be proved from the comparison with our previous flow field study of single-phase steam ejector (See Fig.7 in Ref [14]). Further, Fig. 7b depicts the contours of

fluid pressure, droplet radius r and liquid mass fraction f within the mixing chamber. As one can see, near the secondary nucleation zone, fluid pressure and r decrease to their respective valleys, while f reaches its peak. However, after secondary nucleation, f declines, whereas pressure and r show opposing increasing trends. Additionally, we observed that the secondary nucleation intensity within the mixing chamber, at 1.03×10^{12} $m^{-3}s^{-1}$, is significantly lower than that within the primary nozzle. The maximum f in the secondary nucleation area is 0.13, reaching merely about 85% of the value at the primary nozzle nucleation area. The discrepancies of nucleation intensity and liquid phase distribution between the mixing chamber and primary nozzle underscore the relationship between the fluid expansion strength and the non-equilibrium condensation. Therefore, in the transonic flow of condensable gases, the influencing factors of the non-equilibrium phase transition are various.

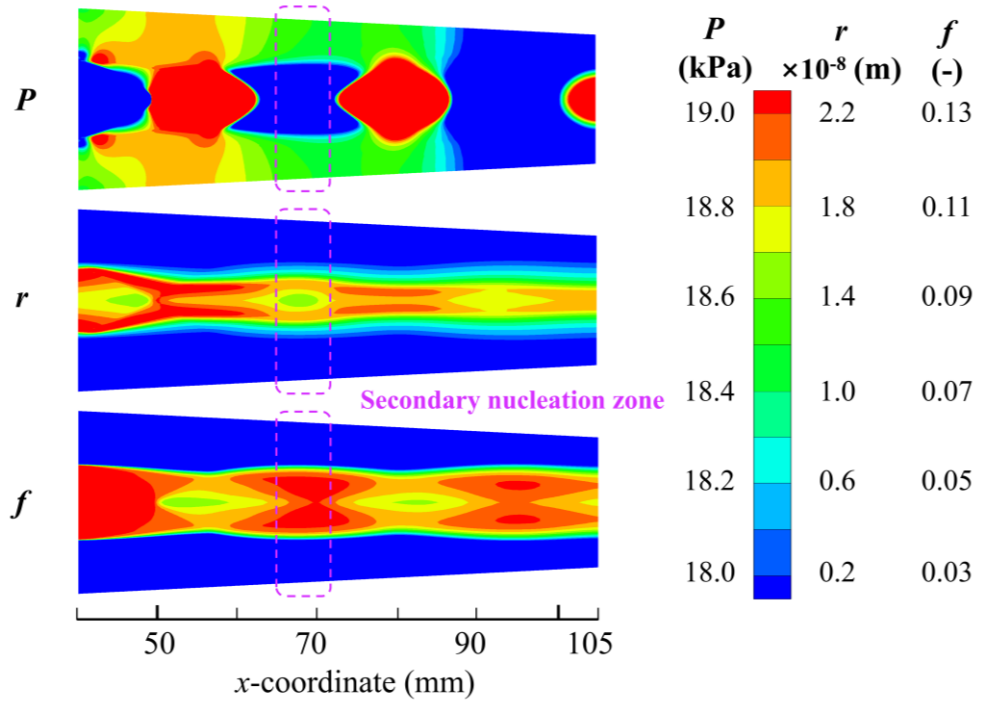

Fig.7b Fluid pressure, droplet radius and liquid mass fraction contour within mixing chamber

4. Operating parameters impact analysis on non-equilibrium phase transition flow

4.1 *Influence of primary fluid pressure P_p*

This section mainly investigates the effects of primary fluid pressure P_p on the non-equilibrium phase transition flow inside the steam ejector. Among that, P_p is varied from 460 kPa to 540 kPa, maintaining the P_s=20 kPa and the P_m=40 kPa constant, the temperature is the saturation temperature at corresponding pressure. The boundary conditions are listed as Case *A* in Table 1.

The ω is a key parameter to reflect the entrainment performance of ejector and is defined as:

$$\omega = \frac{m_s}{m_p} \tag{19}$$

where m_s is the secondary fluid mass flow rate and m_p is the primary fluid mass flow rate.

Fig. 8 shows the variation law of m_p, m_s and ω with P_p under different ejector models. As can be seen, m_p shows a linear increase as P_p increases whether the single-phase or two-phase models are adopted. However, as P_p increases, m_s remains relatively stable in the two-phase model, while in the single-phase model, m_s gradually increased but the growth rate decreased. As a result, the behavior of ω varies between the two models. In the single-phase model, ω initially increases with P_p, and reaches a maximum at P_p=500 kPa which corresponds to optimal ejector performance. Beyond this point, ω decreases. This is because the low-pressure suction contribution caused by the increase of P_p does not offset the additional consumption of primary fluid flow mass. Conversely, the two-phase model consistently shows higher values of ω than the single-phase model within the range of P_p covered. However, ω decreases as P_p increases in the two-phase model. This trend, which differs from the single-phase model, is mainly attributed to the strong irreversible loss from the non-equilibrium phase transition. These losses lead to a severe deterioration in low-pressure suction performance, even though

m_p decreases. As P_p increases, the irreversible loss becomes larger, causing ω to decrease more rapidly.

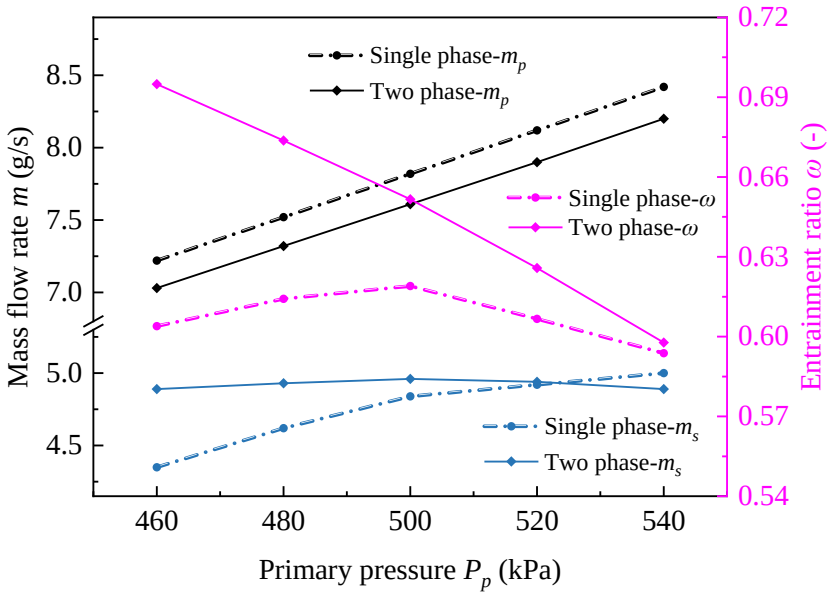

Fig.8 The change of mass flow rate m and entrainment ratio ω under various P_p

To further support the above analysis point of view, Fig. 9 depicts the changing law of liquid mass fraction f and axial pressure distribution with P_p. It is observed that f begins to increase with the occurrence of non-equilibrium condensation, but the differences in the liquid phase distribution within the main nozzle among various P_p are rather small. However, the situation changes after entering the mixing chamber. As P_p increases, f shows a significant increase along the entire path. Its fluctuation amplitude decreases in the mixing chamber but increases in the diffuser. Additionally, the transition positions of the f fluctuation curve shift downstream with P_p increases. The evolution rule of f is highly consistent with the shock wave. For a given primary nozzle, the low-pressure effect induced by the transonic process of saturated steam passing through the main nozzle shows only a slight difference. However, higher P_p leads to greater supersaturation, resulting in an increase in f. The high-pressure primary steam is not fully expanded in the main nozzle and requires further expansion after entering the mixing chamber, which greatly weakens the shock wave intensity. As a result, the fluctuation

amplitude decreases as P_p increases. However, such an under-expanded jet flow will continue to expand at the inlet of diffuser, inducing more significant fluctuations in both the fluid pressure and the f. Moreover, there is a remarkable reduction in f at the end of diffuser, with the rate of decline soaring as P_p decreases, due to the stronger compression effect.

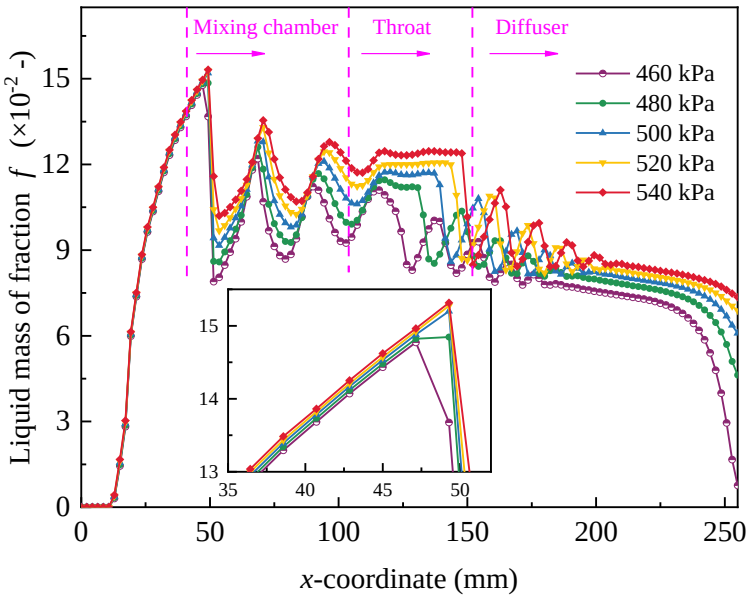

(a) Liquid mass fraction f distributions under various P_p

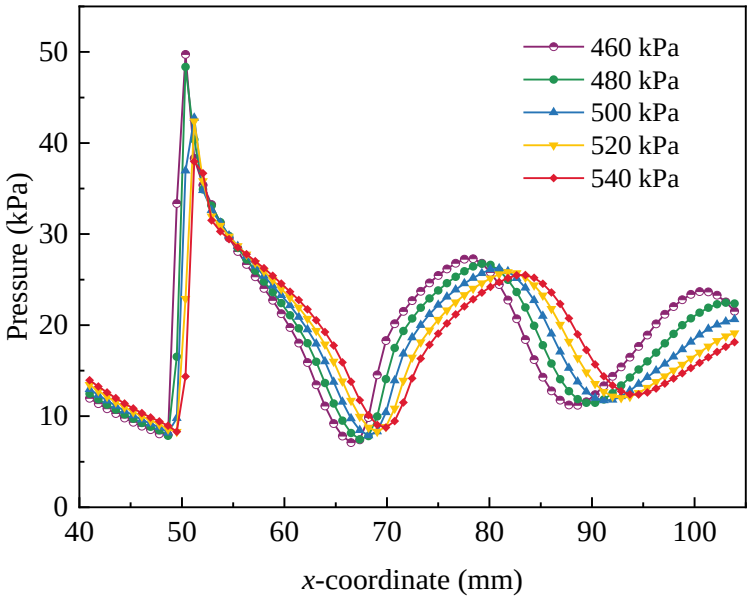

(b) Pressure distributions in mixing chamber under various P_p

Fig.9 Liquid mass fraction f and pressure distributions under various P_p

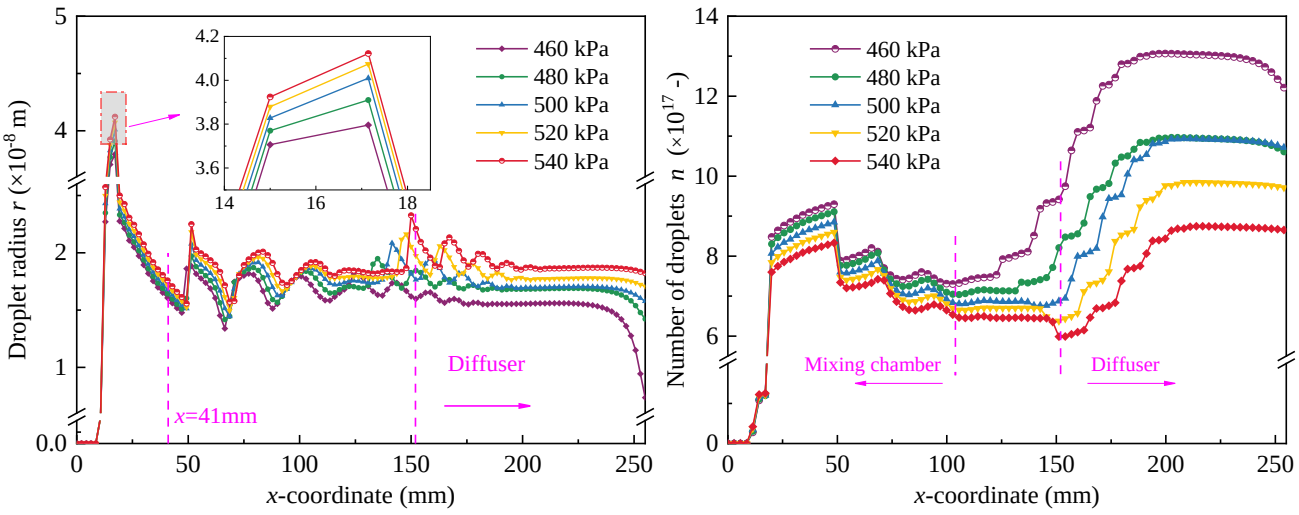

(a) Condensate droplet radius r (b) Condensate droplet number n

Fig.10 Droplet characteristics distributions under various P_p

Fig. 10 shows the dynamic distribution characteristics of droplet under various P_p. As observed, both the condensate droplet radius r and droplets number n increase rapidly, as condensate nucleation occurs inside the main nozzle. Before entering the divergent section of the main nozzle (x=16 mm), r and n are insensitive to changes in P_p, but significant differences emerge thereafter. To be specific, as P_p increase, r becomes larger while n decreases, with the transition positions of these two fluctuation curves shifting downstream. Additionally, stronger fluctuation in r occurs near the entrance of the diffuser with increasing P_p, while the rate of increase in n becomes smaller in this region. At the end of diffuser, r achieves a larger reduction as P_p decrease, while n does not significantly by the stronger compression effect. It is worth pointing out that f and n do not maintain the similar evolution trajectory here as discussed in Section 3.2. The above droplet dynamic distribution characteristics are largely attributed to the effect of shock wave. A stronger shock wave is induced with lower P_p inside the mixing chamber, which would greatly exacerbate the fragmentation and evaporation of the condensate droplets in the primary jet flow. The enhancement of the compression effect at diffuser outlet

contributes to the evaporation of condensate droplets.

4.2 *Influence of secondary fluid pressure P_s*

This section primarily investigates the effects of secondary fluid pressure P_s on the non-equilibrium phase transition inside the steam ejector. Among that, P_s is varied from 16 kPa to 24 kPa, maintaining the P_p=500 kPa and the P_m=40 kPa constant, the temperature is the saturation temperature at corresponding pressure. The boundary conditions are listed as Case *B* in Table 1. It should be pointed that the variation of P_s is very limited and far from breaking the choking flow state inside the nozzle of ejector. That is to say, the variation of P_s has little impact on the flow process inside the nozzle, as well as the phase transition flow characteristic. Furthermore, the mixing of the two fluids becomes increasingly uniform as they progress through the throat and diffuser sections. Therefore, this section only pays close attention to the influences of P_s on the non-equilibrium phase transition flow characteristic inside the mixing chamber.

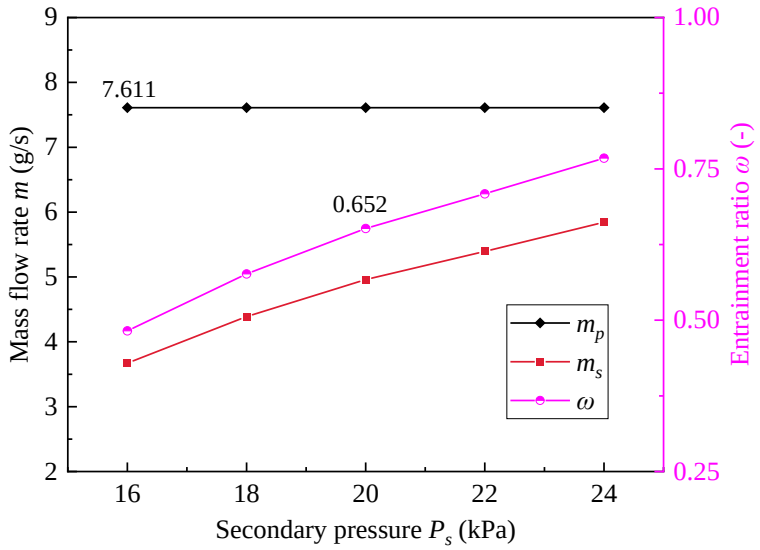

Fig.11 Mass flow rate m and entrainment ratio ω change with various P_s

Fig. 11 illustrates the variation of mass flow rate m and entrainment ratio ω with P_s. It is evident

that the primary fluid mass flow rate m_p remains constant due to the restriction of choking flow. In contrast, the secondary fluid mass flow rate m_s increases with higher P_s, since the suction pressure achieves a significant appreciation. As a result, the entrainment ratio ω increases, with a maximum enhancement of up to 17.8% within the P_s range considered.

To better comprehend the influences of P_s on the non-equilibrium phase transition flow characteristics inside the mixing chamber. Fig. 12 presents the influences of P_s on phase transition flow inside mixing chamber. As one can see, the primary condensate nucleation inside the main nozzle is not subjected to the change of P_s, but the situation is quite different in the secondary nucleation. With an increase in P_s, both the nucleation intensity increases and the nucleation position shifts upstream. Notably, the nucleation phenomenon disappears when P_s drops below 20 kPa. Moreover, as P_s increases, the liquid mass fraction f decreases, and the fluctuation transition position shifts upstream, while the fluctuation amplitude increases.

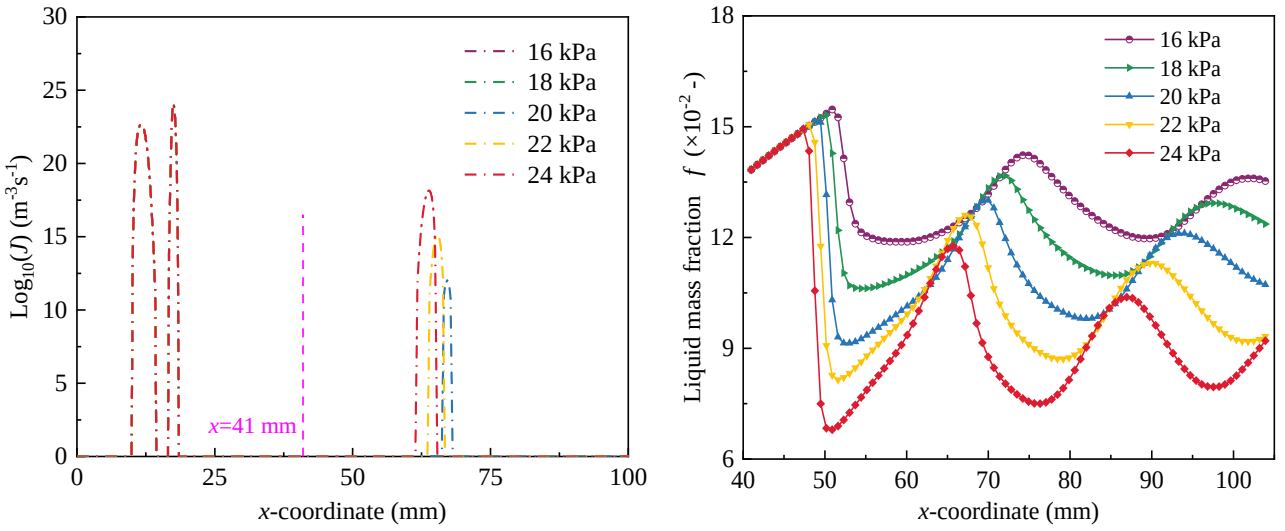

(a) Nucleation rate J (b) Liquid mass fraction f

Fig.12 Influences of P_s on phase transition flow inside mixing chamber

The above evolution rules of phase transition flow can be well explained from the shock wave distribution. As shown in Fig. 13, a stronger shock wave is to be induced as P_s rises, and its fluctuation transition position shifts upstream. The reason is similar to the explanation provided in Section 4.1. Specifically, the low-pressure potential energy of supersonic primary jet flow is more fully utilized, resulting in a smaller supersaturation. Consequently, the shock wave intensity increases, and f accordingly reduces. Furthermore, the secondary expansion wave weakens as P_s decreases, which corresponds to a decrease in secondary nucleation rate J. As P_s continues to decrease, the expansion wave strength is unable to reach the subcooling degree for condensate nucleation, causing secondary nucleation to disappear. A conclusion can be drawn here that the appearance and intensity change of secondary nucleation has a tiny influence on the evolution law of f. Both f and J are primarily subjected to shock wave.

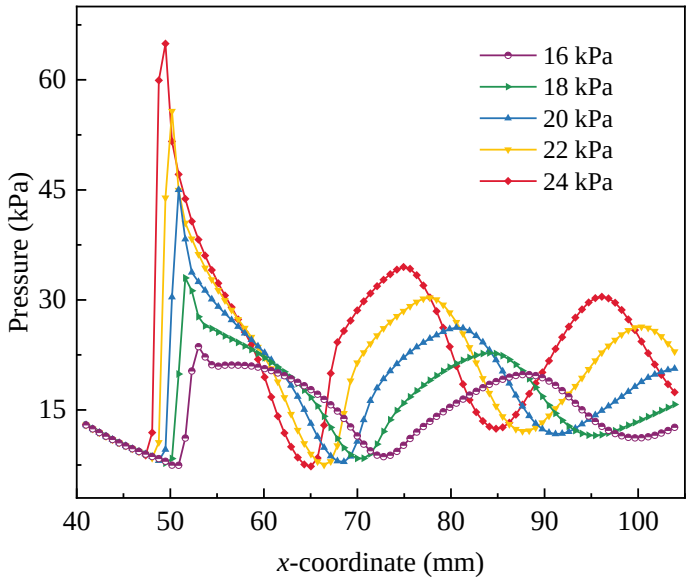

Fig.13 Pressure distributions under various P_s in mixing chamber

Fig. 14 reveals the evolution of condensate droplets inside the mixing chamber under various P_s. It can be seen that both the droplet radius r and the droplet number n exhibit larger fluctuation

amplitude as P_s increases, with the transition positions of these fluctuations shifting upstream. The evolution laws of r and n are essentially dominated by the pressure fluctuation on the shock wave chain, and the reason is the same as discussed in Section 3.2. Moreover, the strong shock wave effect greatly contributes to the fragmentation and extinction of the condensate droplets at high P_s. The appearance of secondary nucleation contributes to an increase in n when P_s exceeds 20 kPa, and this increase becomes more pronounced as P_s rises. One thing is worth noting that this non-equilibrium nucleation is of a short duration, and its intensity is insufficient to alter the evolution law of condensate droplets.

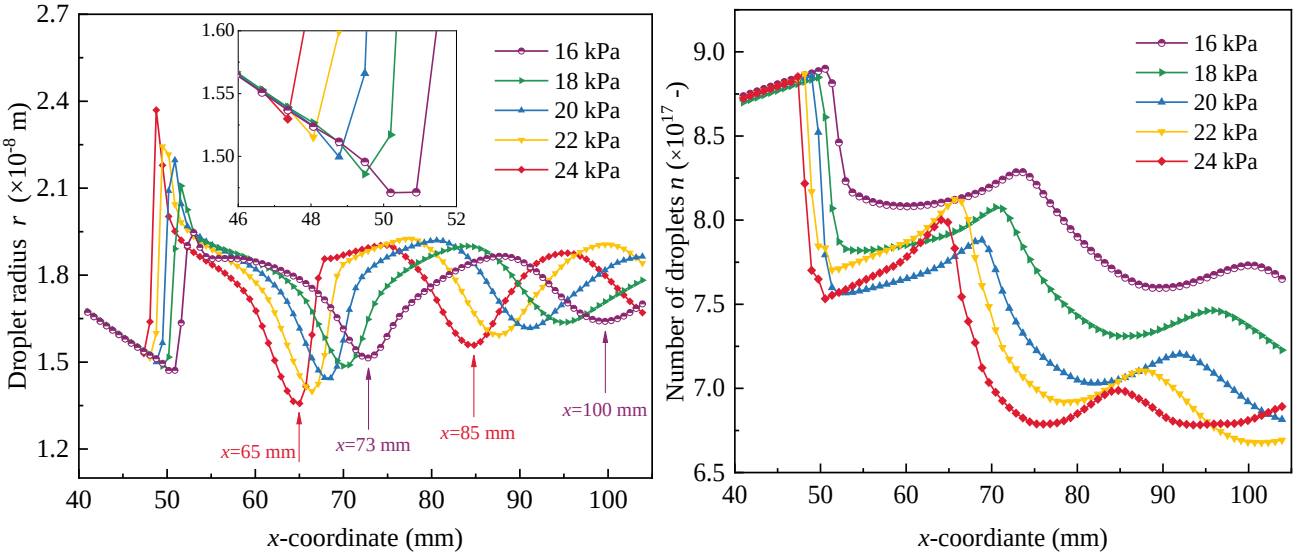

(a) Droplet radius r (b) Number of droplets n

Fig.14 Droplet characteristics distributions under various P_s in mixing chamber

4.3 *Influence of primary fluid superheat degree* ΔT_p

In this section, the influence of primary fluid superheat degree ΔT_p on the non-equilibrium phase transition flow characteristic inside the steam ejector is to be investigated. Among that, ΔT_p is varied form 10 K to 50 K, maintaining the pressure parameters on design conditions. The boundary conditions are listed as Case *D* in Table 1.

Fig. 15 illustrates the change rule of the mass flow rate m, the entrainment ratio ω and the average

of liquid mass fraction f_a with various ΔT_p. It is evident that superheating the primary fluid inhibits the generation and growth of liquid phase, f_a presents a nearly linear decline as ΔT_p rises, and the drop is as high as 42.63%. As a result, the irreversible losses from non-equilibrium phase transition flow reduce, and ω accordingly increases with higher ΔT_p. Among these, the secondary fluid mass flow rate m_s remains relatively stable, while the primary fluid mass flow rate m_p decreases. The decrease of m_p is primarily attributed to the reduction of choking flow as ΔT_p appreciates. It should be noted that overheating of primary fluid has a mild help to the performance improvement of steam ejector. To be specific, the entrainment ratio ω remains close to the design value at ΔT_p=10 K, and even when ΔT_p increases to 50 K, the improvement in ω is only 3.53%. In practical applications, it is essential to carefully balance the cost of fluid overheating with the limited improvement in ejector performance.

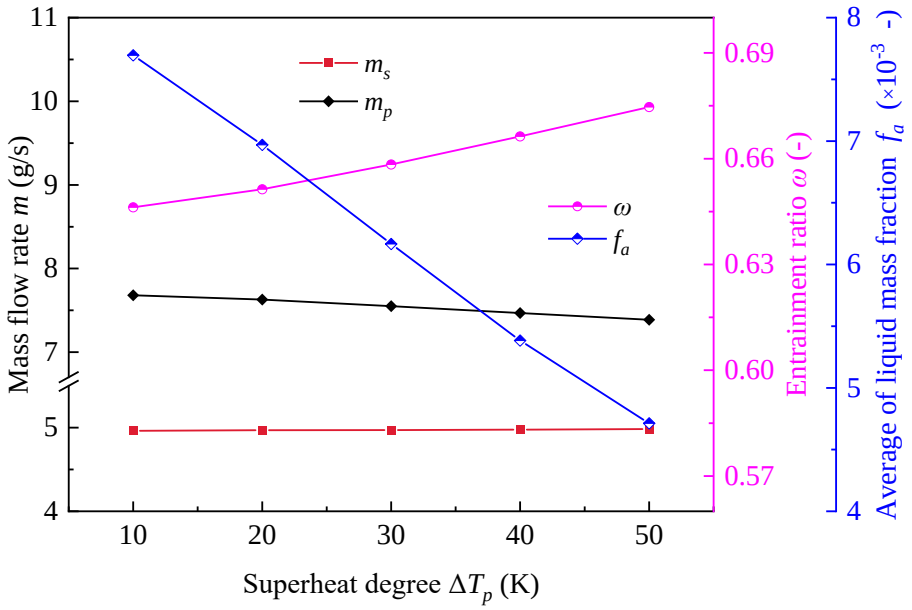

Fig.15 Mass flow rate m, entrainment ratio ω and average of liquid mass fraction f_a change with various ΔT_p

Fig. 16 illustrates the evolution laws of the nucleation rate J and the liquid mass fraction f under varying primary fluid superheat degree ΔT_p. As shown, the primary nucleation region within the main

nozzle gradually narrows as ΔT_p increases, and the nucleation position shifts downstream. It is apparent that the sensitivity of nucleation weakens with overheating, and the original secondary nucleation phenomenon disappears. The evolution laws of the liquid mass fraction f show a high similarity for all ΔT_p cases, i.e., f surges within the main nozzle and then experiences a fluctuating drop after entering the mixing chamber. Additionally, as ΔT_p increases, less condensate is generated inside the steam ejector, and the point where droplets are completely evaporated shifts progressively upstream. The fluctuation amplitude of f becomes slightly larger with higher ΔT_p in the mixing chamber, while the opposite trend occurs near the diffuser inlet. The condensate evolution trajectory downstream of the primary nozzle is mainly influenced by shock wave fluctuation, as previously discussed. As displayed in Fig. 17, the fluctuation amplitude of fluid pressure increases slightly at the mixing chamber as ΔT_p increases, while a slight decrease appears near the diffuser inlet. However, the differences in fluid pressure across various ΔT_p are much smaller compared to the variations observed with P_p and P_s. This just provides a good proof of the evolution law of f.

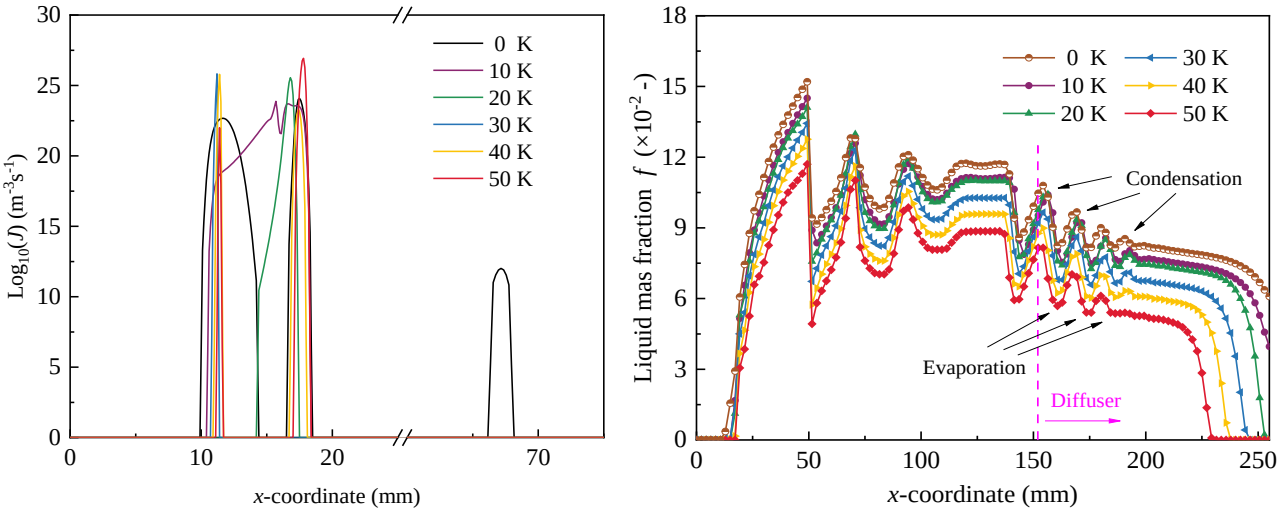

(a) Nucleation rate J (b) Liquid mass fraction f

Fig.16 Nucleation rate J and liquid mass fraction f distributions under various ΔT_p

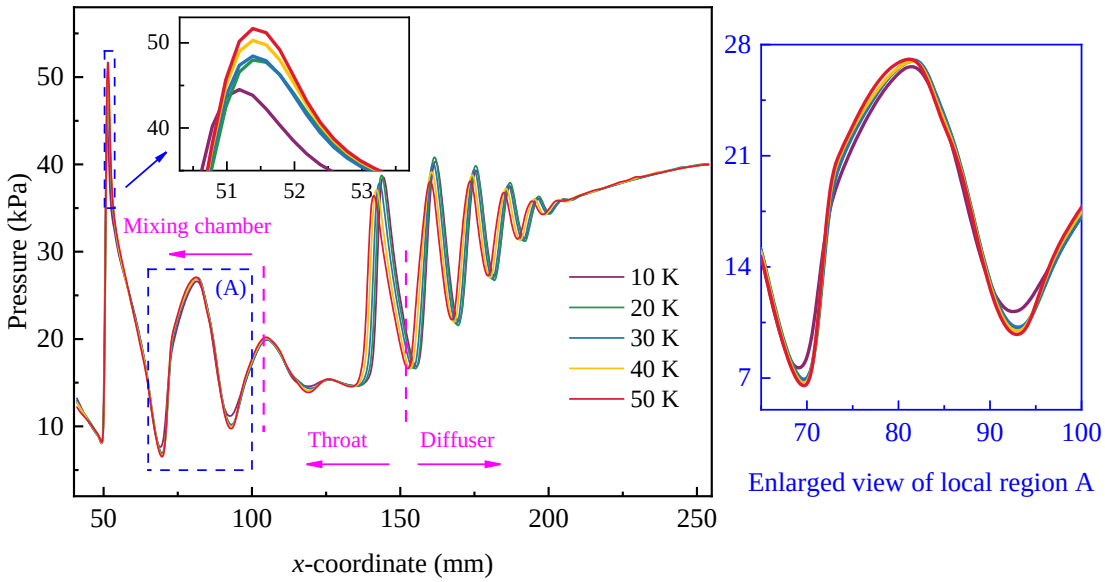

Fig.17 Pressure distributions under various ΔT_p in mixing chamber

Fig. 18 shows more details on the droplet phase transition characteristics under various ΔT_p. It can be observed that a higher ΔT_p contributes to the generation of more condensate droplets with smaller radius, particularly obvious inside the main nozzle. The peak value of r decreases remarkably as ΔT_p increases. To be specific, r drops from 4×10^{-8} m to 2.5×10^{-9} m when the primary fluid is overheated by 50 K. It means that water vapor molecules in the primary fluid are unable to achieve better growth on the existing nucleation, resulting in a decrease in f, even if the numbers of nucleation have a significant appreciation. Moreover, as ΔT_p increases, the fluctuation amplitude of r and the variation in r diminish, while n is the opposite. This phenomenon is not difficult to understand, because fluid overheating largely disrupts the environment of condensate nucleation and droplet growth, and the intensification of internal pressure fluctuations contributes to droplet fragmentation. One interesting thing is that n decreases slightly in the situation of slight overheating, say for example ΔT_p=10 K.

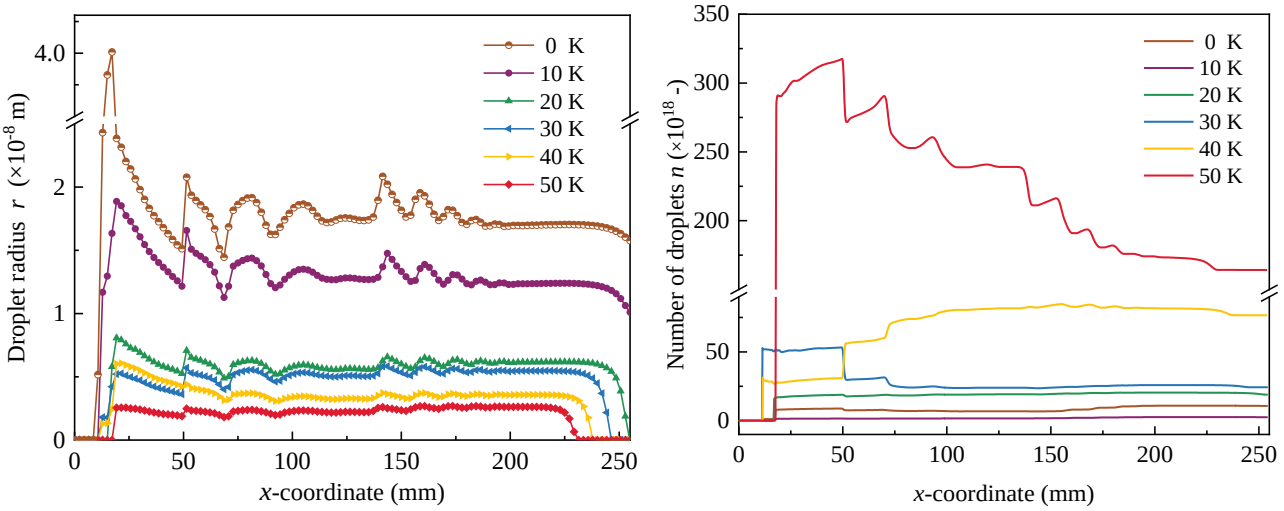

(a) Condensate droplet radius r (b) Condensate droplet number n

Fig.18 Droplet phase transition characteristics distributions under various ΔT_p

4.4 *Influence of secondary fluid superheat degree* ΔT_s

In this section, the influence of secondary fluid superheat degree ΔT_s on the non-equilibrium phase transition flow characteristics inside the steam ejector is to be investigated. Among that, ΔT_s is varied form 10 K to 50 K, and the other boundary conditions are maintained as design value, more details see Case *E* in Table 1.

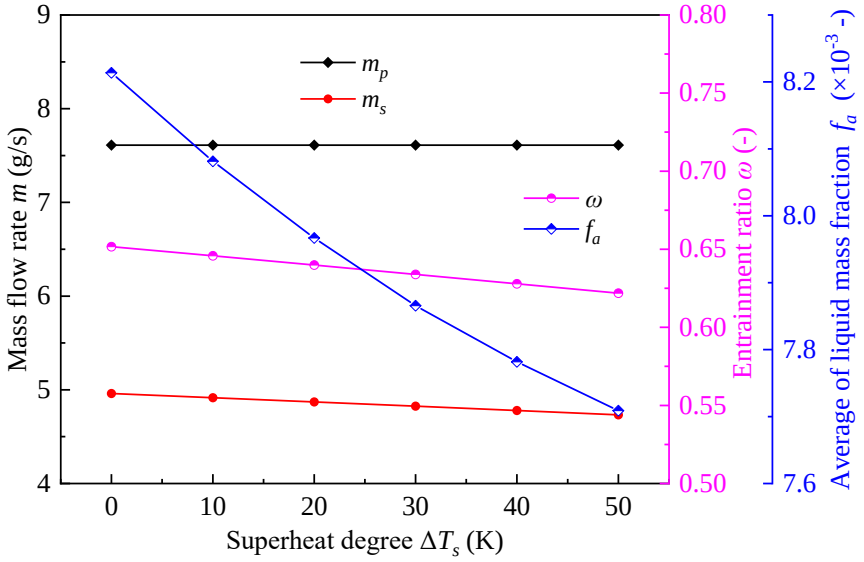

Fig.19 Mass flow rate m, entrainment ratio ω and average of liquid mass fraction f_a change with various ΔT_s

Fig. 19 shows the change rules of mass flow rate m, the entrainment ratio ω and the average of liquid mass fraction f_a with various ΔT_s, where ΔT_s =0 K corresponds the design condition. It is observed that the primary fluid mass flow rate m_p is immune to the change of ΔT_s, whereas the secondary fluid mass flow rate m_s slowly reduces as ΔT_s increases, resulting in a 4.45% decrease of ω. Moreover, the superheating of secondary fluid is capable of depreciating the liquid mass fraction f inside the steam ejector, and f_a reaching a maximum reduction of 6.15% at ΔT_s=50 K.

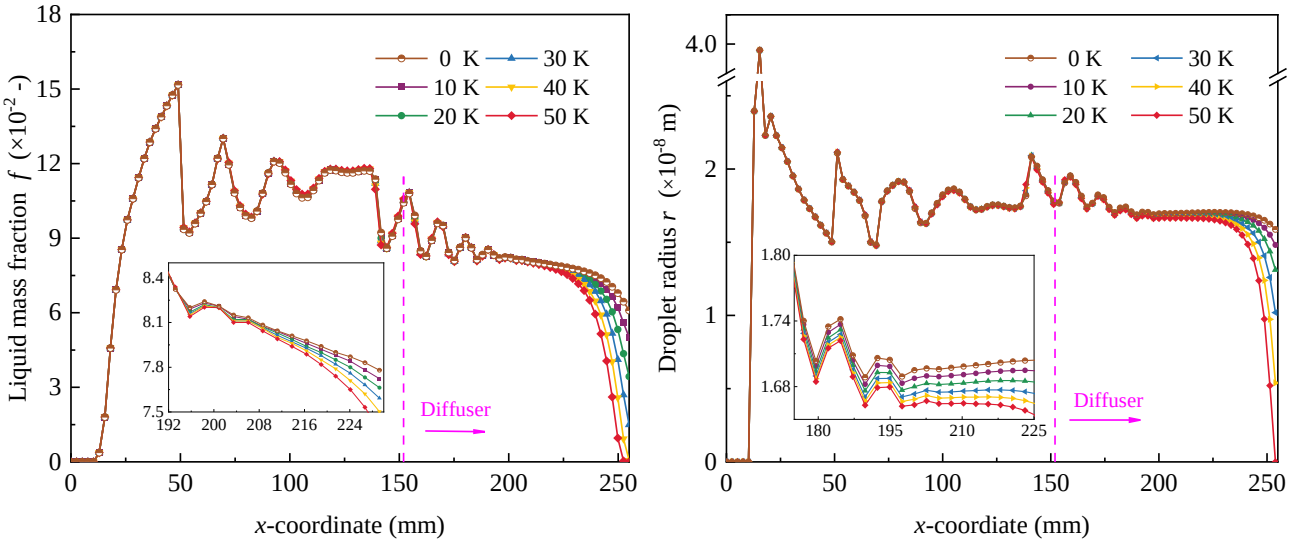

(a) Condensate liquid mass fraction f (b) Condensate droplet radius r

Fig.20 Liquid mass fraction f and droplet radius r distributions under various ΔT_s

Fig. 20 depicts distributions of liquid mass fraction f and droplet radius r under various ΔT_s. As one can see clearly, the superheating of the secondary fluid does not alter the liquid phase distribution upstream of the position x=180 mm, with only a small discrepancy in f and r regardless of ΔT_s. A higher ΔT_s merely contributes to the evaporation of the condensate at the end of diffuser, i.e., f and r rapidly decrease. This means that superheating the secondary fluid has little effect on inhibiting the formation and growth of condensate droplets in the primary jet flow. Consequently, it is not possible to reduce the irreversibility losses from the phase transition flow and improve the entrainment

performance.

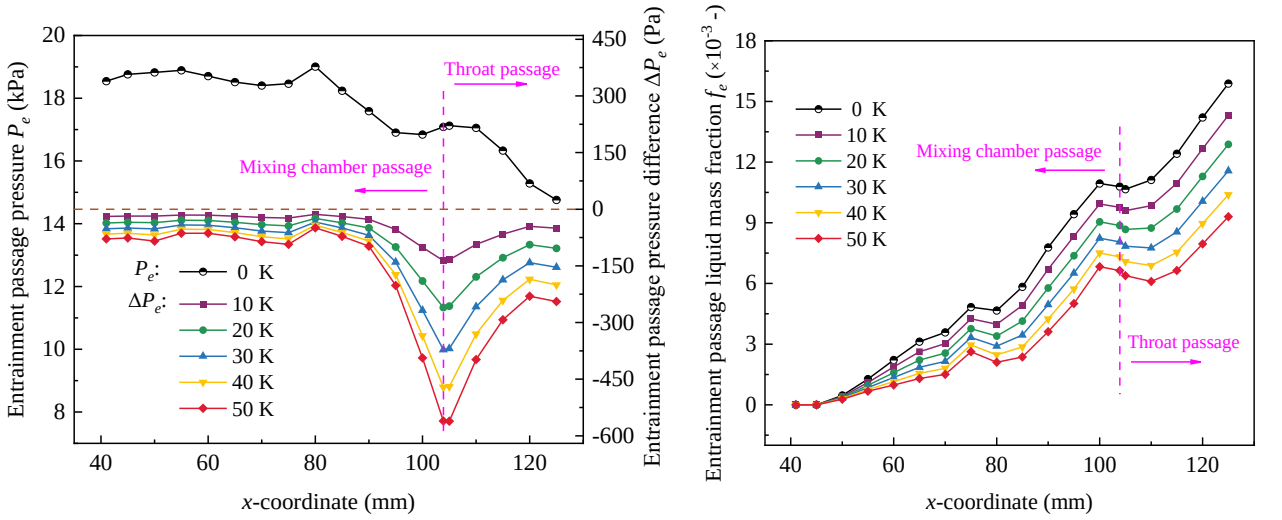

(a) Entrainment passage pressure P_e (b) Entrainment passage liquid mass fraction f_e

Fig.21 Fluid pressure P_e and liquid mass fraction f_e distributions inside entrainment passage under various ΔT_s

Fig. 21 shows distributions of the fluid pressure P_e and liquid mass fraction f_e inside the entrainment passage under various ΔT_s. As one can see, P_e presents a fluctuating decrease along the flow direction at ΔT_s=0 K. Superheating of secondary fluid results in a slight reduction in P_e, and the entrainment passage pressure difference ΔP_e enlarges with higher ΔT_s. It means that the suction driving force of the primary jet flow on the secondary fluid weakens, and the secondary fluid is increasingly difficult to be drawn into the mixing chamber. To be specific, the suction pressure declines by 79 Pa at ΔT_s=50 K, and this value is 18545 Pa at ΔT_s=0 K. Therefore, this results in a deterioration of entrainment performance. Here, ΔP_e is defined as the difference in P_e between the superheating and design conditions. In addition, the superheating of secondary fluid contributes to a reduction of liquid phase inside the entrainment passage, with f_e decreasing with higher ΔT_s. However, the liquid mass fraction in the primary jet flow is far larger than that in the entrainment passage. As a result, the superheating of secondary fluid is unable to penetrate the mixing layer to restrain condensate

generation in the main steam jet. This explains why the evolution trajectory of condensate in the primary jet flow is basically consistent under various ΔT_s (see Fig. 20).

5. Conclusion

In this paper, a considerate two-phase model was developed to explore the formation mechanism and evolution law of non-equilibrium phase transition flow inside the desalination-oriented steam ejector. Additionally, operating parameters impact analysis on both the non-equilibrium phase transition flow and the ejector's entrainment performance are conducted. The key findings are summarized as follows.

(1) During the transonic mixing process, the liquid mass fraction f increases attributed to droplet growth, rather than condensate nucleation. If the expansion wave intensity in the mixing chamber is sufficiently high, secondary condensate nucleation may occur. The expansion wave promotes local condensate droplets to fragment, while the compression wave leads to the aggregation of droplets. The non-equilibrium phase transition is highly sensitive to shock waves, and the variation in f closely follows the pressure fluctuations.

(2) The two-phase model exhibits significant irreversible losses, leading to performance differences when compared to the single-model. As P_p increases, f has a significant increase throughout the path. Moreover, the evolution patterns of the phase transition parameters r and n are opposite, but the amplitude of their fluctuations is notably more intense in both the mixing chamber and diffuser.

(3) As P_s raises, ω achieves a significant increase of 17.8% within the range of P_s. Both the intensities of shock wave and secondary nucleation rise notably, while f decreases. The phenomenon of secondary nucleation disappears when P_s falls below 20 kPa. Moreover, r, n and f present larger

fluctuation amplitude as P_s increases. The induced strong shock effect significantly contributes to the fragmentation and extinction of the condensate droplets.

(4) As ΔT_p increases, the environment of condensate nucleation and droplet growth becomes disrupted. The primary nucleation region narrows, and secondary nucleation disappears. The f_a decreases almost linearly, with a reduction of up to 42.63%. Furthermore, as ΔT_p rises, more small-sized condensate droplets are formed. Fluid overheating leads to a higher ω, but the performance improvement is limited, with a maximum increase of only 3.53%.

(5) Increasing ΔT_s leads to a reduction in the liquid phase inside the entrainment passage and the end of diffuser. The f_a achieves a maximum reduction of 6.15% at ΔT_s=50 K. However, it is hard to restrain the condensate generation in the primary jet flow. Additionally, a slight decrease in fluid pressure occurs inside the entrainment passage, resulting in a modest reduction of 4.45% in ω.

In summary, this study harvests an in-depth understanding of the fundament link among the phase transition flow, shock wave, operating parameters and the entrainment performance of steam ejector. It will be expected to provide important guidance for reducing the ejector's irreversibility loss from the non-equilibrium phase transition flow and optimizing the ejector-associated energy system.

Acknowledgements

This work is supported by National Natural Science Foundation of China (No.52306089), Natural Science Foundation of Jiangxi (No.20224BAB214055 and No.20232BAB204055), Key Research and Development Program of Jiangxi (No.20214ABC28W003), Young Elite Scientists Sponsorship Program by JXAST (2023QT13) and Jingdezhen Social Development Project (No. 20224SF005-05).

References

[1] Tashtoush B M, Al-Nimr M A, Khasawneh M A. A comprehensive review of ejector design, performance, and applications[J]. Applied Energy, 2019, 240: 138-172.

[2] Khan Y, Faruque M W, Nabil M H, et al. Ejector and vapor injection enhanced novel compression-absorption cascade refrigeration system: A Thermodynamic Parametric and Refrigerant Analysis[J]. Energy Conversion and Management, 2023, 289: 117190.

[3] Tang Y Z, Liu Z L, Shi C, et al. A novel steam ejector with pressure regulation to dredge the blocked entrained flow for performance improvement in MED-TVC desalination system[J]. Energy Conversion and Management, 2018, 172: 237-247.

[4] Li H, Wang X D, Huang H L, et al. Numerical study on the effect of superheat on the steam ejector internal flow and entropy generation for MED-TVC desalination system[J]. Desalination, 2022, 537: 115874.

[5] Ding H B, Dong Y Y, Zhang Y, et al. Energy efficiency assessment of hydrogen recirculation ejectors for proton exchange membrane fuel cell (PEMFC) system[J]. Applied Energy, 2023, 346: 121357.

[6] Yu Z S, Liu F, Li C Z. Numerical study on effects of hydrogen ejector on PEMFC performances[J]. Energy, 2023, 285: 129481.

[7] La Torre C A C-D, Velázquez-Limón N, López-Zavala R, et al. High vacuum multiple effect desalination system with barometric ejector condensation[J]. Desalination, 2024, 586: 117842.

[8] Chen J Y, Havtun H, Palm B. Conventional and advanced exergy analysis of an ejector refrigeration system[J]. Applied Energy, 2015, 144: 139-151.

[9] Chen Q, Ja M K, Li Y, et al. Energy, exergy and economic analysis of a hybrid spray-assisted low temperature desalination/thermal vapor compression system[J]. Energy, 2019, 166: 871-885.

[10] Pei P, Ren P, Li Y, et al. Numerical studies on Wide-operating-range ejector based on anodic pressure drop characteristics in proton exchange membrane fuel cell system[J]. Applied Energy, 2019, 235: 729-738.

[11] Wang K, Wang L, Jia L, et al. Optimization design of steam ejector primary nozzle for MED-TVC desalination system[J]. Desalination, 2019, 471: 114070.

[12] Sampedro E.O. A new variable mixing chamber ejector: CFD assessment[J]. Applied Thermal Engineering, 2022, 208: 118242.

[13] Fu W N, Liu Z L, Li Y X, et al. Numerical study for the influences of primary steam nozzle distance and mixing chamber throat diameter on steam ejector performance[J]. International Journal of Thermal Sciences, 2018, 132: 509-516.

[14] Tang Y Z, Li Y X, Liu Z L, et al. A novel steam ejector with auxiliary entrainment for energy conservation and performance optimization[J]. Energy Conversion and Management, 2017, 148: 210-221.

[15] Opgenorth M J, Sederstrom D, McDermott W, et al. Maximizing pressure recovery using lobed nozzles in a supersonic ejector[J]. Applied Thermal Engineering, 2012, 37: 396-402.

[16] Tang Y Z, Liu Z L, Li Y X, et al. Visualization experimental study of the condensing flow regime in the transonic mixing process of desalination-oriented steam ejector[J]. Energy Conversion and Management, 2019, 197: 111849.

[17] Zhang G J, Dykas S, Li P, et al. Accurate condensing steam flow modeling in the ejector of the Solar-driven refrigeration system[J]. Energy, 2020, 212: 118690.

[18] Bian J, Cao X W, Yang W, et al. Condensation characteristics of natural gas in the supersonic liquefaction process[J]. Energy, 2019, 168: 99-110.

[19] Li Y Q, Shen S Q, Yang Y. Three-dimensional characteristics of aerodynamic shockwave and condensation

shockwave in steam ejectors[J]. Desalination, 2024, 581: 117606.

[20] Han Q Y, Feng H D, Zhang H L, et al. Model optimization and mechanism analysis of two-stage ejector considering nonequilibrium condensation[J]. Energy, 2024, 310: 133271.

[21] Zhang G J, Zhang X Z, Wang D B, et al. Performance evaluation and operation optimization of the steam ejector based on modified model[J]. Applied Thermal Engineering, 2019, 163: 114388.

[22] Zhang G J, Dykas S, Yang S C, et al. Optimization of the primary nozzle based on a modified condensation model in a steam ejector[J]. Applied Thermal Engineering, 2020, 171: 115090.

[23] Tashtoush B, Alshare A, Al-Rifai S. Performance study of ejector cooling cycle at critical mode under superheated primary flow[J]. Energy Conversion and Management, 2015, 94: 300-310.

[24] Tang Y Z, Yuan J L, Liu Z L, et al. Study on evolution laws of two-phase choking flow and entrainment performance of steam ejector oriented towards MED-TVC desalination system[J]. Energy, 2022, 242: 122967.

[25] Yang Y, Zhu X W, Yan Y Y, et al. Performance of supersonic steam ejectors considering the nonequilibrium condensation phenomenon for efficient energy utilisation[J]. Applied Energy, 2019, 242: 157-167.

[26] Wen C, Ding H B, Yang Y. Performance of steam ejector with nonequilibrium condensation for multi-effect distillation with thermal vapour compression (MED-TVC) seawater desalination system[J]. Desalination, 2020, 489: 114531.

[27] Wen C, Gong L, Ding H B, et al. Steam ejector performance considering phase transition for multi-effect distillation with thermal vapour compression (MED-TVC) desalination system[J]. Applied Energy, 2020, 279: 115831.

[28] Ding H B, Zhao Y F, Wen C, et al. A visual mass transfer study in the ejector considering phase change for multi-effect distillation with thermal vapour compression (MED-TVC) desalination system[J]. Desalination,

2022, 532: 115722.

[29] Aliabadi M A F, Bahiraei M. Effect of water nano-droplet injection on steam ejector performance based on non-equilibrium spontaneous: A droplet number study[J]. Applied Thermal Engineering, 2021, 184: 116236.

[30] Feng H D, Yao A L, Han Q Y, et al. Effect of droplets in the primary flow on ejector performance of MED-TVC systems[J]. Energy, 2024, 293: 130741.

[31] Ding H B, Dong Y Y, Zhang Y, et al. Exergy performance analysis of hydrogen recirculation ejectors exhibiting phase change behaviour in PEMFC applications[J]. Energy, 2024, 300: 131563.

[32] Ghorbani S, Deymi-Dashrebayza M, Tayyeban E. Parametric investigation and performance optimization of a MED-TVC desalination system based on 1-D ejector modeling[J]. Energy Conversion and Management, 2023, 288: 117131.

[33] Li Y F, Deng J Q, Ma L, et al. Visualization of two-phase flow in primary nozzle of a transcritical CO_2 ejector[J]. Energy Conversion and Management, 2018, 171: 729-741.

[34] Palacz M, Bodys J, Haida M, et al. Two-phase flow visualisation in the R744 vapour ejector for refrigeration systems[J]. Applied Thermal Engineering, 2022, 210: 118322.

[35] Kantrowitz A. Nucleation in very Rapid Vapor Expansions[J]. The Journal of Chemical Physics, 1951, 19(9): 1097-1100.

[36] Wróblewski W, Dykas S, Gepert A. Steam condensing flow modeling in turbine channels[J]. International Journal of Multiphase Flow, 2009. 35(6): 498-506.

[37] Young J B. An equation of state for steam for turbomachinery and other flow calculations[J]. Journal of Engineering for Gas Turbines and Power, 1988, 110(1): 1-7.

[38] Young J B. Two-Dimensional, Nonequilibrium, Wet-Steam Calculations for Nozzles and Turbine Cascades[J].

Journal of Turbomachinery, 1992, 114(3): 569-579.

[39] Bartosiewicz Y, Aidoun Z, Desevaux P, et al. Numerical and experimental investigations on supersonic ejectors[J]. International Journal of Heat Fluid Flow, 2005, 26: 56-70.

[40] Wen C, Karvounis N, Walther J H, et al. An efficient approach to separate CO_2 using supersonic flows for carbon capture and storage[J]. Applied Energy, 2019, 238: 311-319.

[41] Śmierciew C, Gagan J, Butrymowicz D. Application of numerical modelling for design and improvement of performance of gas ejector[J]. Applied Thermal Engineering, 2019, 149: 85-93.

[42] Moses C A, Stein G D. On the Growth of Steam Droplets Formed in a Laval Nozzle Using Both Static Pressure and Light Scattering Measurements[J]. Journal of Fluids Engineering, 1978, 100(3): 311-322.

[43] Al-Doori G. Investigation of refrigeration system steam ejector performance though experiments and computational simulations[D]. Australia: University of Southern Queensland, 2013: 103-109.